

Enhanced single-photon emission from a diamond–silver aperture

Jennifer T. Choy^{1†}, Birgit J. M. Hausmann^{1†}, Thomas M. Babinec^{1†}, Irfan Bulu^{1†}, Mughees Khan², Patrick Maletinsky³, Amir Yacoby³ and Marko Lončar^{1*}

Solid-state quantum emitters, such as the nitrogen-vacancy centre in diamond¹, are robust systems for practical realizations of various quantum information processing protocols^{2–5} and nanoscale magnetometry schemes^{6,7} at room temperature. Such applications benefit from the high emission efficiency and flux of single photons, which can be achieved by engineering the electromagnetic environment of the emitter. One attractive approach is based on plasmonic resonators^{8–13}, in which sub-wavelength confinement of optical fields can strongly modify the spontaneous emission of a suitably embedded dipole despite having only modest quality factors. Meanwhile, the scalability of solid-state quantum systems critically depends on the ability to control such emitter–cavity interaction in a number of devices arranged in parallel. Here, we demonstrate a method to enhance the radiative emission rate of single nitrogen-vacancy centres in ordered arrays of plasmonic apertures that promises greater scalability over the previously demonstrated bottom-up approaches for the realization of on-chip quantum networks.

Efficient single-photon generation and extraction from solid-state quantum emitters is an important problem to be overcome in quantum photonic devices and systems. In the case of devices based on the nitrogen-vacancy (NV) centre in diamond, the photon generation rate and out-coupling efficiency are limited by the relatively long radiative lifetime and total internal reflection (TIR) at the diamond/air interface. Approaches to overcome this issue have therefore been focused on two fronts: enhancement of the radiative decay rate and improvement of the overall collection efficiency. The latter has been realized by direct fabrication of nanowires¹⁴ and solid-immersion lenses^{15–17} in bulk diamond crystals, allowing the collected single-photon count rates to be increased by roughly an order of magnitude. The spontaneous emission rate and intrinsic radiance of the colour centre can be improved by means of the Purcell effect, which can be achieved by coupling diamond nanocrystals¹⁸ or nanopillars to evanescent or confined optical fields produced by dielectric^{19–24} or metallic^{25–28} nanostructures. Given the maturity of diamond nanofabrication techniques, it has also recently become possible to thin bulk diamond membranes to optically thick slabs on which planar resonators with embedded colour centres could be fabricated^{29,30}.

A bottleneck in many of these techniques is the deterministic coupling of single quantum emitters to photonic elements, which is typically challenging and incompatible with large-scale production of devices. For instance, bottom-up approaches involving diamond nanocrystals have predominantly relied on random (drop/spin-casting) or alignment-sensitive (pick-and-place by an atomic force microscope tip) techniques of positioning diamond nanocrystals to achieve emitter–optical field coupling, resulting in

one-of-a-kind devices. Although top-down nanofabrication has been shown to provide a reliable and high-throughput means to generate large arrays of devices^{14,31,32}, the demonstrated structures have thus far mainly focused on improving the out-coupling efficiency without modification of the radiative lifetime. In this Letter, we present a high-yield approach to directly embed single NV centres into metallic nanostructures, leading to a reduction in the spontaneous emission lifetime of the enclosed NV centres. Specifically, we consider plasmonic apertures (Fig. 1a) consisting of cylindrical diamond nanoposts (radius, $r \approx 50$ nm; height, $h \approx 180$ nm) surrounded by silver. These structures support modes with mode volumes as small as $0.07(\lambda/n)^3$ and can provide good spatial overlap between the highly localized optical fields and enclosed dipole due to nearly uniform field distributions in the transverse direction (Fig. 1b,c). This results in enhancement of the spontaneous emission rate of the dipole.

The spontaneous emission rate enhancements for our structures were calculated with a three-dimensional finite-difference time-domain (3D FDTD) solver using a classical approach¹³ by comparing the total power emitted from a dipole when it is placed inside the aperture to the total power emitted in a homogeneous medium. The simulations were performed with measured parameters from ref. 33 and take into account material losses in the silver. The theoretical spontaneous emission rate enhancement spectrum, plotted in Fig. 1d for aperture radii of 50, 55 and 65 nm, exhibits a broad resonance that redshifts with increasing radius and can therefore be tailored to overlap with the NV emission while keeping the height of the structure constant¹³. Based on our simulations, enhancements of the spontaneous emission rate on the order of ~ 30 can be expected for a radially polarized NV centre placed at the maximum field intensity in an optimized structure.

The hybrid diamond–metal device depicted in Fig. 1a was realized using a combination of blanket ion implantation and top-down nanofabrication techniques^{14,31,32} (Fig. 2a). Two ultrapure bulk diamond crystals (type IIa, Element 6) were used. The samples were implanted with nitrogen ions and subsequently annealed to generate a layer of NV centres roughly 20 nm and 90 nm below the diamond surface. Arrays of diamond nanoposts with radii from 50 nm to 70 nm and height of ~ 180 nm were then fabricated using electron-beam lithography followed by inductively coupled plasma reactive ion etching (ICP RIE) (Fig. 2b). We have previously shown³² that such a procedure can result in a high yield ($>10\%$) of single-centre devices. The nanoposts were finally embedded in a 500-nm-thick silver film that was deposited by electron-beam evaporation. The thickness of the silver layer was chosen to ensure that the diamond nanoposts were fully covered and to minimize oxidation of silver at the device layer.

¹School of Engineering and Applied Sciences, Harvard University, Cambridge, Massachusetts 02138, USA, ²Wyss Institute, Harvard University, Cambridge, Massachusetts 02138, USA, ³Department of Physics, Harvard University, Cambridge, Massachusetts 02138, USA; [†]These authors contributed equally to this work. *e-mail: loncar@seas.harvard.edu

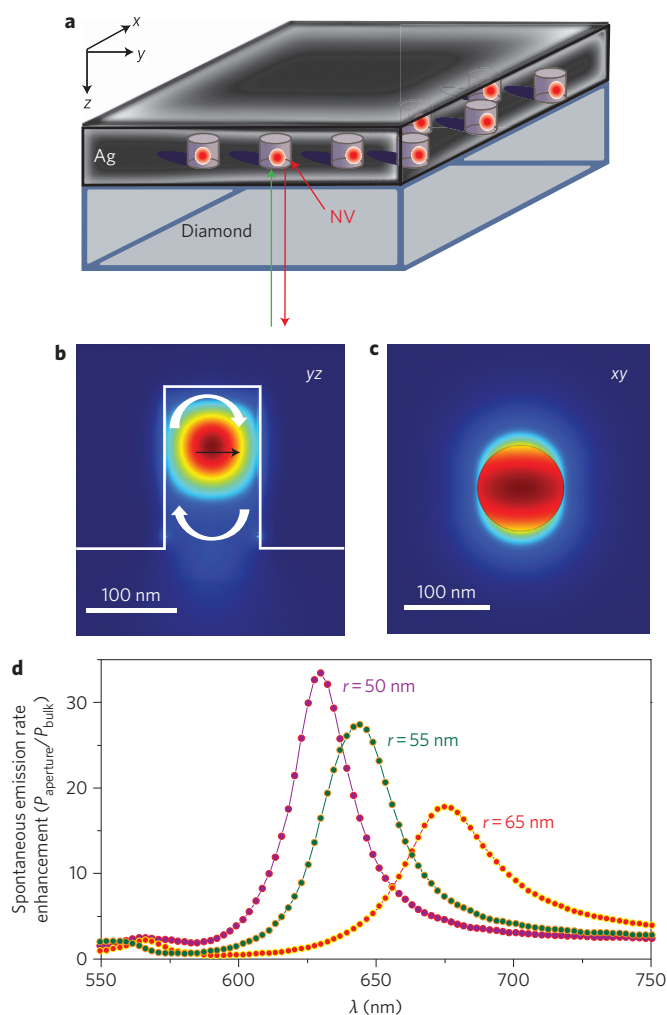


Figure 1 | Single-photon source based on diamond-plasmon apertures.

a, Three-dimensional schematic of the diamond-plasmonic system. The idealized structure for coupling to the NV emission consists of a diamond nanopost (height, ~ 180 nm; diameter, ~ 100 nm) embedded in a 500-nm-thick layer of silver. NV fluorescence is excited and collected through the bulk part of the diamond sample (green and red arrows, respectively). **b**, Cross-sectional view of the structure along either the x - z (or y - z) plane, plotted with the longitudinal mode profile. The dipole is shown to be radially polarized and positioned in the centre of the structure, where field density is maximized. As in a Fabry-Pérot resonator, light reflects off the diamond-metal interfaces (curved arrows) and becomes tightly confined in the nanoposts. **c**, Simulated lateral (x - y) mode profile shows a near-uniform energy distribution of the plasmonic mode. **d**, Simulated spontaneous emission enhancement as a function of wavelength for nanoposts with different radii, calculated by placing the dipole at the field maximum.

To rigorously quantify the effect of the plasmon cavity on single NV centres, we identified bare nanoposts containing single NV centres and compared their emission properties before and after silver deposition for the 20-nm-implant sample. These optical characterizations were performed under ambient conditions using a home-built confocal microscope with a modest numerical aperture ($NA \approx 0.6$) and long working distance ($WD \approx 4$ mm), which allowed us to optically access plasmonic nanostructures through the 500- μm -thick bulk diamond material (Fig. 2c). A comparison between confocal scans taken on an array of $r \approx 65$ nm posts before (Fig. 2d) and after (Fig. 2e) silver deposition under identical experimental conditions indicated enhancement of light emission

by the nanoposts in the presence of the silver. The nature of photon emission was then further characterized by autocorrelation measurements to determine photon statistics and triggered fluorescence decay measurements³² to extract lifetime information.

For the 20-nm-implant sample, we tested a total of 65 silver-embedded nanoposts of radii 50 nm and 65 nm, and measured the autocorrelation function of each enclosed emitter, $g^{(2)} = \langle I(t)I(t+\tau) \rangle / \langle I(t) \rangle^2$, as a function of time delay τ , in a Hanbury Brown and Twiss experiment. Of these, five devices exhibited single-photon character, with $g^{(2)}(0) < 0.5$ (Fig. 3, from the circled post in Fig. 2e). No background subtraction was performed in all data presented. In addition to the preservation of non-classical behaviour, we observed significant narrowing of the anti-bunching dips in comparison to those taken for nanoposts before silver deposition at the same excitation power (Fig. 3a), which suggests an enhancement of the spontaneous emission rate due to the plasmonic cavity. However, this comparison does not take into account possible changes in the excitation rate of the NV centre due to the presence of silver, so quantitative comparison of the spontaneous emission rates was subsequently performed by means of lifetime measurements. A further 13 devices showed some degree of anti-bunching, with $0.5 < g^{(2)}(0) < 1$, although many of these had previously exhibited single-photon emission in the absence of silver. The reductions in $g^{(2)}$ contrast in these cases may be due to plasmon-enhanced background fluorescence from the silver film. Indeed, this background luminescence was observed in spectrally resolved photoluminescence measurements performed on an 'empty' aperture (without NV centre). To improve the quality of our silver films, we used a titanium adhesion layer (thickness, 2 nm) between the diamond and silver in the 90-nm-implant sample.

The spontaneous emission rate enhancement was investigated by time-resolved photoluminescence measurements. Pulsed excitation was used to trigger an exponentially decaying fluorescence signal from which the lifetime information was extracted. The ensemble averaged lifetime of the densely populated NV centres in an unstructured area on the 20-nm-implant sample was measured to be 16.7 ± 0.5 ns, while the bare posts (without silver) exhibited quenched NV emission leading to much longer lifetimes, with average values of 33.3 ± 7.5 ns for $r \approx 65$ nm and 38.3 ± 7.3 ns for $r \approx 50$ nm nanoposts containing single NV centres (Fig. 3c). Additionally, the longest lifetime we measured for the bare nanoposts was 47.57 ± 1.1 ns, suggesting that such a system could be advantageous for experiments requiring prolonged excited states³⁴. The increase in lifetime with decreasing post radius is due to the reduced density of states for the radiative transition as a result of the nanostructuring³⁵ and corroborates FDTD simulations based on measured post dimensions. Our calculations also indicate that the nanopost geometry leads to quenching of spontaneous emission for both the radial and axial components of the dipole, although the dominant contribution to the collected photons is the radial polarization.

After silver deposition, the lifetimes of the NV centres implanted at 20 nm were shortened by maximum factors of 6.6 for $r \approx 65$ nm posts and 4.8 for $r \approx 50$ nm posts and were observed to be as short as 5.2 ns. For the 90-nm-implant sample, lifetimes as short as 2.4 ns were measured, corresponding to roughly a sixfold decrease over the bulk lifetime. A comparison of fluorescence decays measured for a representative device before and after silver deposition is shown in Fig. 3d. The enhancement in spontaneous emission rate is accompanied by an increase in the count rates that can be observed in saturation measurements. For direct comparison, we examined one set of measurements on the same 50 nm post before and after silver deposition. In this case, we found that the bare and silver-enhanced saturation intensities (and lifetimes) were $(6.1 \pm 0.2) \times 10^3$ counts per second (c.p.s.) (42.4 ± 0.8 ns) and $(4.4 \pm 0.2) \times 10^4$

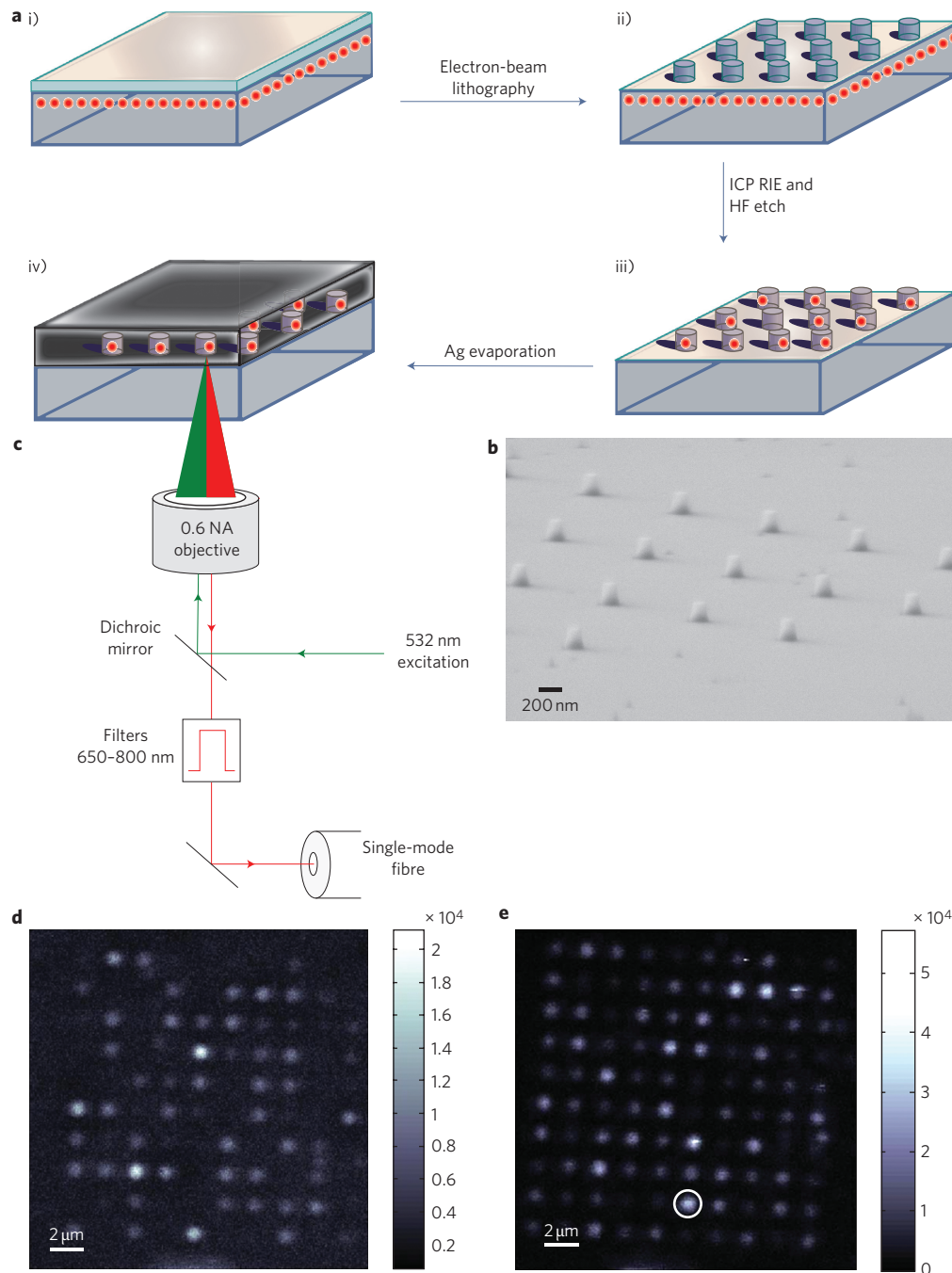


Figure 2 | Fabrication and optical microscopy of devices. **a**, Illustration of fabrication procedure: (i) resist spinning on bulk diamond after nitrogen implantation and annealing, (ii) mask definition by electron-beam lithography, (iii) pattern transfer to the diamond substrate in an oxygen-based RIE, and (iv) capping of the shallow implanted diamond posts in silver (after resist removal). Optical characterization was performed after both steps (iii) and (iv) on the same set of posts to measure the extent of plasmonic enhancement. **b**, Scanning electron microscopy image of a representative array of diamond posts after step (iii) in **a**. **c**, Schematic of experimental configuration for sample characterization. **d,e**, Confocal microscopy scans of the same array of $r \approx 65$ nm posts before (**d**) and after (**e**) silver deposition with identical pump power. The circled post represents a plasmon-enhanced device containing a single NV centre. The spacing between adjacent posts is $2 \mu\text{m}$.

c.p.s. (9.26 ± 0.1 ns), respectively. Therefore, the enhancements in spontaneous emission rate and fluorescence intensity are, respectively, 4.6 and 7.3. Because the lifetime reduction was accompanied by a comparable increase in the photon count rate, the observed plasmonic enhancement can be attributed to radiative processes. However, additional factors might be at play in contributing to a slight increase in the collection efficiency of the silver-capped device, such as out-coupling (scattering) of surface plasmon

modes at the diamond/silver interface due to the surface roughness of the metal. In comparison to single NV centres in the bulk measured using the same low-NA set-up (data not shown), the measured saturation intensities are approximately two to three times higher, with the best 20-nm-implant diamond plasmon device (Fig. 3e) saturating at $(1.01 \pm 0.02) \times 10^5$ c.p.s. at a saturation power of 1.18 ± 0.06 mW. In general, saturation measurements were difficult to carry out in the shallow-implanted nanoposts, as

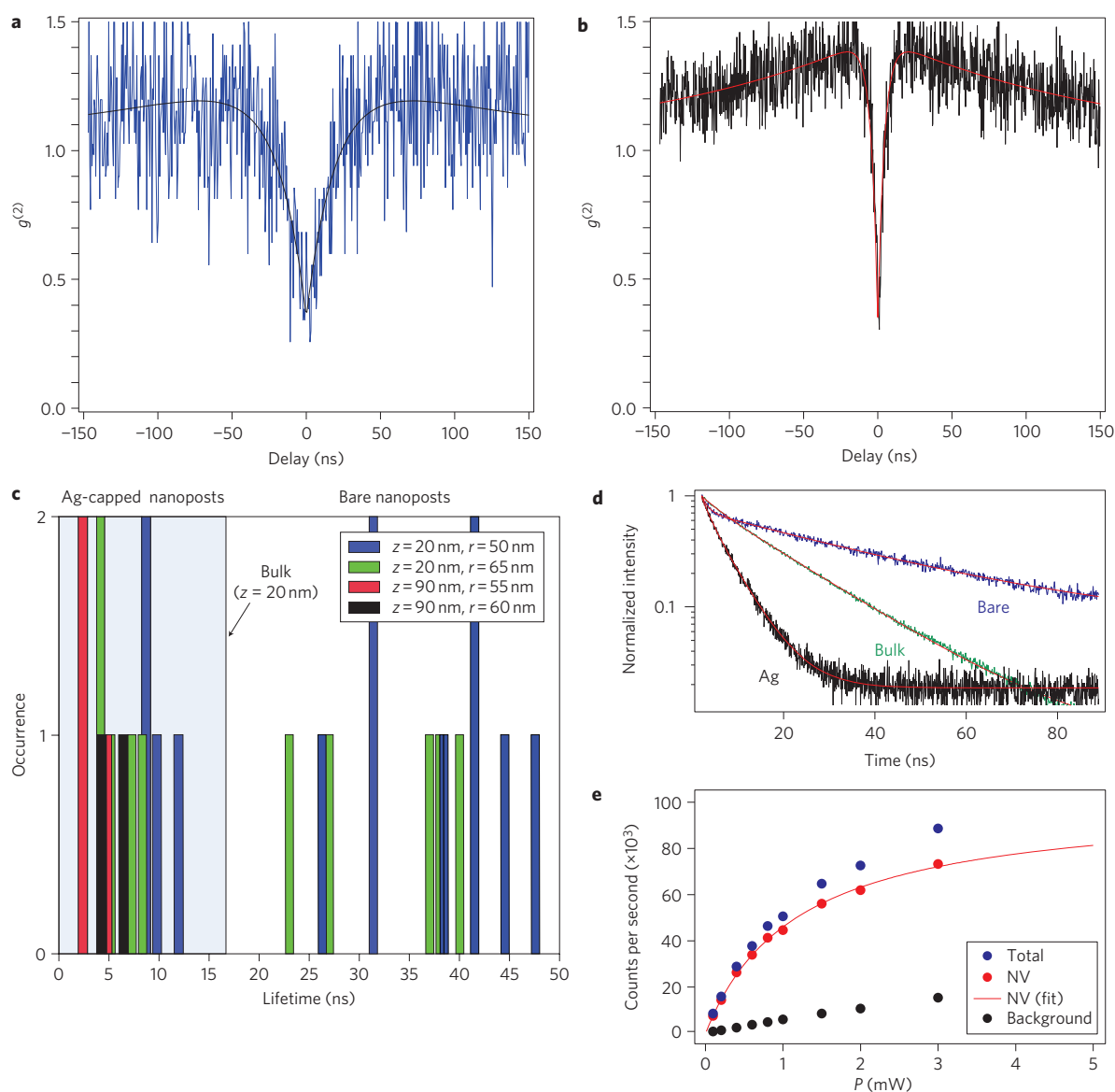


Figure 3 | Spontaneous emission enhancement of single NV centres. **a,b**, Autocorrelation function for a representative bare nanopost (**a**) and a silver-embedded device (**b**) (circled in Fig. 2d) reveal strong anti-bunching at zero time delay, indicating emission of non-classical light. No background subtraction was performed. The grey and red curves in **a** and **b**, respectively, represent fits to the $g^{(2)}$ function¹. **c**, Histogram of NV centre lifetimes for nanoposts of different radii r and implantation depths z before and after silver deposition. The shaded region represents data points for silver-capped posts, and the measured bulk lifetime for NV centres implanted 20 nm below the diamond surface is denoted with a grey line. The quenching of light emission in the bare nanoposts is due to the reduced density of states in the nanostructures. **d**, Normalized fluorescence decays for the same $r \approx 65$ nm nanopost, containing a single NV centre, before and after silver deposition and for an ensemble population of NV centres in the bulk region, together with fits to a multi-exponential model (shown in red). The fits yielded time constants for fast-decaying background fluorescence (< 2 ns) as well as a slower NV photoluminescence (bare, 37.17 ± 0.7 ns; silver-embedded, 5.65 ± 0.08 ns; bulk, 16.7 ± 0.08 ns). **e**, Saturation curve for a silver-embedded nanopost with an NV centre implanted at 20 nm. The total count rates are shown as blue dots, and the background contributions (measured from an empty post without any NV centres) are given as black dots. Subtraction of the background from the total yields the NV emission (red dots), which can be fitted to the saturation model (solid line). The fitted saturation intensity and power are $(1.01 \pm 0.02) \times 10^5$ c.p.s. and 1.18 ± 0.06 mW.

photo-ionization of the NV centres could occur at high excitation powers ($P > 2$ mW), so that the saturation intensities could only be inferred from fitting to the saturation model. In addition to TIR at the diamond/air interface, photon losses in the system can be attributed to coupling of emitted photons to surface plasmons, which propagate laterally on the diamond/silver surface and could not be collected. Indeed, FDTD calculations show that only 4–5% of the emitted photons are captured by the collection optics, which suggests that further structural optimization, such as the addition of gratings, might be necessary to increase the number of collected photons¹³.

Photoluminescence spectra taken for the silver-embedded nanoposts consisted of NV centre emission and first- and second-order Raman signals from the diamond (not shown). Resonance peaks could be observed after subtracting the background photoluminescence (from an empty post) from the plasmon-enhanced NV-centre spectrum. For the 90-nm-implanted nanoposts shown in Fig. 4a, the quality factors are ~ 10 , with central peak wavelengths redshifting from 665.5 nm to 718.9 nm with increasing radius from 50 nm to 70 nm. The dispersion in resonances between similarly sized posts ($r \approx 55$ nm) can be explained by the sensitivity of the

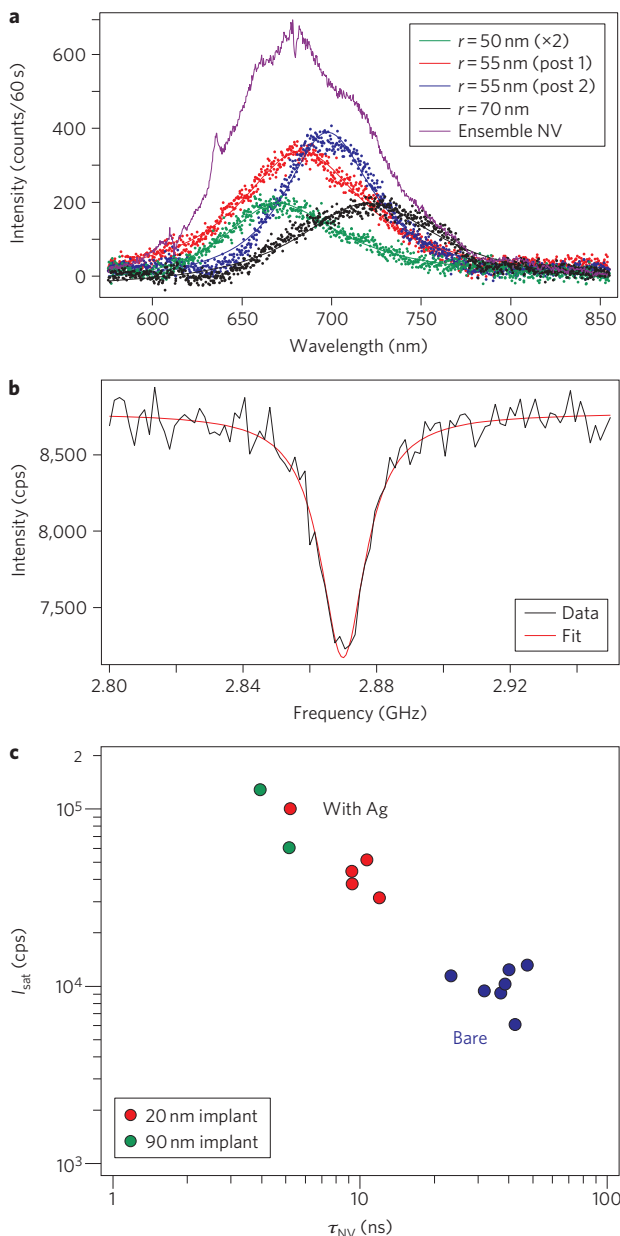


Figure 4 | Comparison of photoluminescence spectra and device performances. **a**, Background-subtracted spectra for four different devices in the 90-nm-implant sample, together with a reference NV centre spectrum taken from an ensemble of NV centres in a silver-covered, unstructured region of the sample. Each solid line represents the fit to the raw data (dots). The $r \approx 50$ nm nanopost was integrated for twice as long (120 s). The quality factors corresponding to the fits lie roughly between 7 (black curve) and 11 (blue curve), and the resonance peaks range from 665.5 nm ($r \approx 50$ nm post) and 718.9 nm ($r \approx 70$ nm post). **b**, Optically detected magnetic resonance spectrum of a plasmon-enhanced NV centre, measured by tuning the microwave source over the NV centre splitting between the $m_s = 0$ and $m_s = \pm 1$ ground-state levels without an external magnetic field. The spectrum reveals a characteristic dip at 2.87 GHz and a contrast of 18.3%. **c**, Performance plot of saturation intensity as a function of fluorescence lifetime for the bare and silver-capped devices tested for this study, showing that the plasmonic enhancement provided by the geometry has led to shorter lifetimes and correspondingly higher count rates.

resonance to nanoscale deviations in the dimensions of different devices (Fig. 1d). Finally, the observed fluorescence was unequivocally assigned to NV-centre emission using room-temperature

optically detected electron spin resonance (ESR) measurements³⁶. We observed a characteristic NV-ESR spectrum (Fig. 4b) with a dip in fluorescence at an applied microwave frequency of 2.87 MHz and a fluorescence contrast of 18.3%. Although the preservation of contrast compared to measurements on bulk NV centres suggests the viability of spin systems based on plasmon-enhanced NV emission, a critical property for both quantum information and magnetometry is spin coherence, which will have to be addressed in future experiments. However, spin coherence time can generally be extended substantially using dynamical decoupling techniques³⁷.

To illustrate the overall performance improvement, we plotted saturation intensity against lifetime for a number of devices, bare and silver-capped, at the two implantation depths. Figure 4c shows a significant decrease in the lifetimes of the silver-capped devices, accompanied by an enhancement in photon emission. For our best 20-nm-deep device, the Purcell enhancement is 6.4 and 3.2 compared to average lifetimes for the bare nanopost and unstructured shallow implanted NV centres, respectively. We also modelled the fabricated devices using dimensions obtained from scanning electron microscopy imaging (Fig. 2b). In addition to the geometry (the truncated conical shapes of the finished devices), the modelling took into account the implantation depth and straggle, as well as ambiguity in the polarization angle of the dipole moment arising from phonon mixing due to the [100] orientation of the diamond crystal plane³⁸. From these considerations, we determined the spectrally averaged minima and maxima of the enhancements in the spontaneous emission rate in the 20-nm-implant sample to be 2 and 3.6 in comparison to the bulk (shallow-implanted), showing a good convergence with experimental values. Moreover, the degree of spontaneous emission enhancement is maximized when the dipole is placed at the centre of the aperture, and drops off as its axial position deviates from the field maximum, so larger Purcell enhancements (Fig. 1d) are anticipated with optimized implantation depth. Indeed, devices on the 90-nm-implant sample show that the NV centre lifetime can be shortened to 2.4 ns, which represents an approximately sixfold decrease over bulk values. Finally, modified device designs¹³ will allow for collimated emission, resulting in larger collection efficiencies of emitted photons.

The method presented here provides controlled coupling in a quantum emitter–plasmonic resonator system, for a large number of devices arranged in parallel, and has yielded Purcell-enhanced single-photon emission of NV centres. In comparison to existing bottom-up approaches, our geometry is scalable and can be implemented without alignment-sensitive procedures. Such diamond–plasmon devices can therefore serve as a basis and proof of principle for more complex diamond–plasmon structures¹³ that can potentially provide stable and reliable systems for demonstrating enhanced zero-phonon line (ZPL) of the NV centre, long-range coupling between qubits via surface plasmons³⁹, and improved optical readouts for single spin states.

Methods

Fabrication. The arrays of nanoposts used in this experiment were fabricated on electronic-grade, type IIa CVD diamond samples, which were implanted with nitrogen ions (at an energy of 14 keV and a dose of $1.25 \times 10^{12} \text{ cm}^{-2}$ for the 20 nm implant, and 75 keV and $1.5 \times 10^{11} \text{ cm}^{-2}$ for the 90 nm implant) and subsequently annealed under high vacuum ($<10^{-9}$ torr) at 750 °C (20 nm) and 800 °C (90 nm) for 2 h. The substrates were cleaned in a boiling 1:1:1 nitric/perchloric/sulphuric acid bath before resist spinning (XR electron-beam resist, Dow Corning). Arrays of circular patterns (radii, 50–70 nm) were then defined using an electron-beam lithography system (Elionix) at 100 kV. After developing the resist (in 25% tetramethyl ammonium hydroxide), the sample was subject to an ICP RIE oxygen dry etch to transfer the mask patterns onto the diamond substrate, resulting in ~ 180 -nm-tall nanoposts. The samples were then placed in hydrofluoric acid and the nitric/perchloric/sulphuric acid bath to remove the residual mask as well as any contaminants from processing. Finally, a 500-nm-thick silver film was deposited on the nanoposts by electron-beam evaporation (Denton). For the 90-nm-implant sample, a 2-nm-thick evaporated layer of titanium was added before silver deposition.

Characterization. The optical performance of the nanoposts, before and after silver deposition, was tested in a home-built confocal microscope. For the autocorrelation and saturation measurements, a continuous-wave 532 nm laser was used for excitation and focused through the diamond sample onto individual posts using an air objective (Olympus LUCPlanFLN $\times 40$, NA = 0.6), and both the incoming and collected signals were scanned by a steering mirror (Newport). Emitted light collected by the objective passed through a dichroic mirror and was then spectrally and spatially filtered using bandpass filters (650–800 nm) and a single-mode fibre (2×2 coupler, Thorlabs) before being sent to avalanche photodiodes (Perkin Elmer) for photodetection and measurement of photon statistics. Spectral data were acquired using a grating spectrometer (Jobin Yvon iHR550, 76 mm \times 76 mm monochromator with 150 g mm⁻¹ gratings).

Pulsed excitations used to trigger the decaying fluorescence signals were generated by passing ultrafast (~ 200 fs) pulses at ~ 800 nm from a Ti:sapphire laser (Coherent) through a photonic-crystal fibre (Newport). The resulting supercontinuum white light was spectrally filtered using bandpass filters between 510 and 540 nm (Semrock) to generate green pulses. For lifetime measurements requiring longer time periods between pulses, the 76 MHz repetition rate of the Ti:sapphire pulse train was reduced to ~ 10.8 MHz using an electro-optic modulator (ConOptics) before launching into the photonic-crystal fibre. All time-correlated measurements were performed using a time-correlated single-photon-counting module (PicoHarp).

ESR measurements were performed using a confocal microscope with a 0.8NA objective. Microwaves were applied using a semirigid coaxial cable, which was shorted with a 25- μ m-diameter gold bonding wire loop. The gold wire was approached from the bottom side of the sample in close proximity to the silver film (30–40 μ m distance). Bulk silver has a skin depth of 1.2 μ m at 2.8 GHz, and our 500 nm silver film was therefore largely transparent to the applied radiofrequency field. Additionally, the reduced conductivity of the evaporated silver film further enhanced its transparency to microwaves. A Rohde Schwarz SMB 100A microwave generator was used and the signal was amplified with a 30 dB gain in a Minicircuits ZHL-42W.

Received 27 April 2011; accepted 23 August 2011;
published online 9 October 2011

References

- Kurtsiefer, C., Mayer, S., Zarda, P. & Weinfurter, H. Stable solid-state source of single photons. *Phys. Rev. Lett.* **85**, 290–293 (2000).
- Beveratos, A. *et al.* Single photon quantum cryptography. *Phys. Rev. Lett.* **89**, 187901 (2002).
- Jelezko, F. *et al.* Observation of coherent oscillation of a single nuclear spin and realization of a two-qubit conditional quantum gate. *Phys. Rev. Lett.* **93**, 130501 (2004).
- Childress, L. *et al.* Coherent dynamics of coupled electron and nuclear spin qubits in diamond. *Science* **314**, 281–285 (2006).
- Gurudev Dutt, M. V. *et al.* Quantum register based on individual electronic and nuclear spin qubits in diamond. *Science* **316**, 1312–1316 (2007).
- Maze, J. R. *et al.* Nanoscale magnetic sensing with an individual electronic spin in diamond. *Nature* **455**, 644–648 (2008).
- Balasubramanian, G. *et al.* Nanoscale imaging magnetometry with diamond spins under ambient conditions. *Nature* **455**, 648–652 (2008).
- Ebbesen, T. W., Lezec, H. J., Ghaemi, H. F., Thio, T. & Wolff, P. A. Extraordinary optical transmission through sub-wavelength hole arrays. *Nature* **391**, 667–669 (1998).
- Rigneault, H. *et al.* Enhancement of single-molecule fluorescence detection in subwavelength apertures. *Phys. Rev. Lett.* **95**, 117401 (2005).
- Akimov, A. V. *et al.* Generation of single optical plasmons in metallic nanowires coupled to quantum dots. *Nature* **450**, 402–406 (2007).
- Kolosev, R. *et al.* Wave-particle duality of single surface plasmon polaritons. *Nature Phys.* **5**, 470–474 (2009).
- Maksymov, I. S. *et al.* Metal-coated nanocylinder cavity for broadband nonclassical light emission. *Phys. Rev. Lett.* **105**, 180502 (2010).
- Bulu, I., Babinec, T., Hausmann, B., Choy, J. T. & Loncar, M. Plasmonic resonators for enhanced diamond NV- center single photon sources. *Opt. Express* **19**, 5268–5276 (2011).
- Babinec, T. M. *et al.* A diamond nanowire single-photon source. *Nature Nanotech.* **5**, 195–199 (2010).
- Hadden, J. P. *et al.* Strongly enhanced photon collection from diamond defect centres under microfabricated integrated solid immersion lenses. *Appl. Phys. Lett.* **97**, 241901 (2010).
- Siyushev, P. *et al.* Monolithic diamond optics for single photon detection. *Appl. Phys. Lett.* **97**, 241902 (2010).
- Schröder, T., Gädeke, F., Banholzer, M. J. & Benson, O. Ultrabright and efficient single-photon generation based on nitrogen-vacancy centres in nanodiamonds on a solid immersion lens. *New J. Phys.* **13**, 055017 (2011).
- Beveratos, A., Brouri, R., Gacoin, T., Poizat, J.-P. & Grangier, P. Nonclassical radiation from diamond nanocrystals. *Phys. Rev. A* **64**, 061802(R) (2001).
- Park, Y.-S., Cook, A. K. & Wang, H. Cavity QED with diamond nanocrystals and silica microspheres. *Nano Lett.* **6**, 2075–2079 (2006).
- Larsson, M., Dinyari, K. N. & Wang, H. Composite optical microcavity of diamond nanopillar and silica microsphere. *Nano Lett.* **9**, 1447–1450 (2009).
- Englund, D. *et al.* Deterministic coupling of a single nitrogen vacancy center to a photonic crystal cavity. *Nano Lett.* **10**, 3922–3926 (2010).
- Santori, C. *et al.* Nanophotonics for quantum optics using nitrogen-vacancy centers in diamond. *Nanotechnology* **21**, 274008 (2010).
- Sar, T. v. d. *et al.* Deterministic nano-assembly of a coupled quantum emitter-photonic crystal cavity system. *Appl. Phys. Lett.* **98**, 193103 (2011).
- Barclay, P. E., Santori, C., Fu, K.-M., Beausoleil, R. G. & Painter, O. Coherent interference effects in a nano-assembled diamond NV center cavity-QED system. *Opt. Express* **17**, 8081–8097 (2009).
- Schietinger, S., Barth, M., Aichele, T. & Benson, O. Plasmon-enhanced single photon emission from a nanoassembled metal/diamond hybrid structure at room temperature. *Nano Lett.* **9**, 1694–1698 (2009).
- Schell, A. W. *et al.* Single defect centers in diamond nanocrystals as quantum probes for plasmonic nanostructures. *Opt. Express* **19**, 7914–7920 (2011).
- Huck, A., Kumar, S., Shakoor, A. & Andersen, U. L. Controlled coupling of a single nitrogen-vacancy center to a silver nanowire. *Phys. Rev. Lett.* **106**, 096801 (2011).
- Chi, Y., Chen, G., Jelezko, F., Wu, E. & Zeng, H. Enhanced photoluminescence of single-photon emitters in nanodiamonds on a gold film. *IEEE Photon. Tech. Lett.* **23**, 374–376 (2011).
- Faraon, A., Barclay, P. E., Santori, C., Fu, K.-M. C. & Beausoleil, R. G. Resonant enhancement of the zero-phonon emission from a colour centre in a diamond cavity. *Nature Photon.* **5**, 301–305 (2011).
- Hausmann, B. M. *et al.* On-chip single crystal diamond resonators. *CLEO/QELS 2011*, Baltimore, MD, 5 May (2011).
- Hausmann, B. *et al.* Fabrication of diamond nanowires for quantum information processing applications. *Diam. Relat. Mater.* **19**, 621–629 (2010).
- Hausmann, B. J. M. *et al.* Single color centers implanted in diamond nanostructures. *New J. Phys.* **13**, 045004 (2011).
- Johnson, P. B. & Christy, R. W. Optical constants of the noble metals. *Phys. Rev. B* **6**, 4370–4379 (1972).
- Fuchs, G. D. *et al.* Excited-state spin coherence of a single nitrogen-vacancy centre in diamond. *Nature Phys.* **6**, 668–672 (2010).
- Chew, H. Radiation and lifetimes of atoms inside dielectric particles. *Phys. Rev. A* **38**, 3411–3416 (1988).
- Gruber, A. *et al.* Scanning confocal optical microscopy and magnetic resonance on single defect centers. *Science* **276**, 2012–2014 (1997).
- de Lange, G., Wang, Z. H., Risté, D., Dobrovitski, V. V. & Hanson, R. Universal dynamical decoupling of a single solid-state spin from a spin bath. *Science* **330**, 60–63 (2010).
- Fu, K.-M. C. *et al.* Observation of the dynamic Jahn-Teller effect in the excited states of nitrogen-vacancy centers in diamond. *Phys. Rev. Lett.* **103**, 256404 (2009).
- Gonzalez-Tudela, A. *et al.* Entanglement of two qubits mediated by one-dimensional plasmonic waveguides. *Phys. Rev. Lett.* **106**, 020501 (2011).

Acknowledgements

The authors thank D. Twitchen and M. Markham from Element Six for providing diamond samples, and C.L. Yu, P. Hemmer and O. Bakr for helpful discussions. The authors also thank K.P. Chen and V. Shalaev for their helpful suggestions. T.M.B. acknowledges support from the National Defense Science and Engineering Graduate (NDSEG) and National Science Foundation (NSF) Graduate Research fellowships, and J.T.C. acknowledges support from the NSF Graduate Research fellowship. Devices were fabricated in the Center for Nanoscale Systems (CNS) at Harvard. This work was supported in part by Harvard University's Nanoscale Science and Engineering Center (NSEC), a NSF Nanotechnology and Interdisciplinary Research Team grant (ECCS-0708905), the Defense Advanced Research Projects Agency (Quantum Entanglement Science and Technology program), and the King Abdullah University of Science and Technology Faculty Initiated Collaboration Award (FIC/2010/02).

Author contributions

J.T.C., B.J.M.H. and T.M.B. performed the experiments and analysed the data. I.B. developed the theory and numerically modelled the structures. B.J.M.H. and J.T.C. fabricated the devices. M.K. contributed insights on the fabrication. P.M. and A.Y. provided additional experimental apparatus and helped with the measurements. M.L. and I.B. supervised the project. J.T.C., B.J.M.H. and M.L. wrote the paper. All authors discussed the results and commented on the manuscript.

Additional information

The authors declare no competing financial interests. Reprints and permission information is available online at <http://www.nature.com/reprints>. Correspondence and requests for materials should be addressed to M.L.